International Journal of Bioprinting

RESEARCH ARTICLE

Hybrid solid mesh structure for electron beam melting customized implant to treat bone cancer

Jong Woong Park[1,2,3†], Eunhyeok Seo[4†], Haeum Park[5], Ye Chan Shin[2], Hyun Guy Kang[1], Hyokyung Sung[6*], Im Doo Jung[4*]

[1]Orthopaedic Oncology Clinic, Center for Rare Cancers, National Cancer Center, Goyang 10408, Republic of Korea

[2]Surgical Oncology Branch, Division of Clinical Research, National Cancer Center, Goyang 10408, Republic of Korea

[3]Department of Cancer Control and Population Health, NCC-Graduate School of Cancer Science and Policy, National Cancer Center, Goyang 10408, Republic of Korea

[4]Department of Mechanical Engineering, Ulsan National Institute of Science and Technology, UNIST-gil 50, Ulsan, 44919, Republic of Korea

[5]Department of 3D Printing Materials, Korea Institute of Materials Science, Changwon, 51508, Republic of Korea

[6]Department of Materials Science and Engineering, Kookmin University, Seoul 02707, Republic of Korea

(This article belongs to the *Special Issue: Laser bioprinting technologies*)

[†]These authors contributed equally to this work.

***Corresponding authors:**
Hyokyung Sung
(hyokyung@kookmin.ac.kr)

Im Doo Jung
(idjung@unist.ac.kr)

Citation: Park JW, Seo E, Park H, *et al*., 2023, Hybrid solid mesh structure for electron beam melting customized implant to treat bone cancer. *Int J Bioprint*, 9(4): 716. https://doi.org/10.18063/ijb.716

Received: November 03, 2022
Accepted: February 02, 2023
Published Online: March 21, 2023

Abstract

Bone replacement implants manufactured by electron beam melting have been widely studied for use in bone tumor treatment. In this application, a hybrid structure implant with a combination of solid and lattice structures guarantees strong adhesion between bone and soft tissues. This hybrid implant must exhibit adequate mechanical performance so as to satisfy the safety criteria considering repeated weight loading during the patient's lifetime. With a low volume of a clinical case, various shape and volume combinations, including both solid and lattice structures, should be evaluated to provide guidelines for implant design. This study examined the mechanical performance of the hybrid lattice by investigating two shapes of the hybrid implant and volume fractions of the solid and lattice structures, along with microstructural, mechanical, and computational analyses. These results demonstrate how hybrid implants may be designed to improve clinical outcomes by using patient-specific orthopedic implants with optimized volume fraction of the lattice structure, allowing for effective enhancement of mechanical performance as well as optimized design for bone cell ingrowth.

***Keywords*:** 3D printing; Bone cancer; Titanium alloy implant; Electron beam melting; Fracture analysis

1. Introduction

The limb salvage surgery is one of the treatment processes for bone sarcoma that resects bone tumors with wide margins and reconstructs bone and soft-tissue defects. Endoprosthesis and biological substitutes, such as bone allografts or recycled autografts, are the most common methods for replacing bone defects after wide excision[1-4]. There are limitations on using allografts or conventional implants as a treatment for a malignant tumor, which can occur anywhere in the body and in various sizes. Consequently, using a customized implant in patients undergoing extensive tissue removal can be an alternative method.

Additive manufacturing (AM) technology has been extensively developed in various fields[5-9]. The development of AM has allowed for the innovative design of patient-specific orthopedic implants for bone sarcoma patients[10-15]. This current technology can replace the allograft with a 3D-printed implant and combine an endoprosthesis with an implant in limb salvage surgery[16]. Conventional modular-type tumor implants often require total replacement of the whole joint with an artificial joint to fix the implant, resulting in disability for the patient. In contrast, AM can preserve the patient's joint if the tumor does not erode the adjacent joint[17,18].

Despite the advantages mentioned above, the mechanical performance of the implant produced by AM must meet the rigid endurance and safety criteria. The load direction and magnitude of the implant depend on the surgical site; the lower limb has to withstand repeated weight loads more than the upper limb. Moreover, to regenerate bone and soft tissues and ensure strong adhesion to the bone tissues, the implant should be composed of hybrid structures that combine solid and lattice structures. The lattice structure with an open porosity inside the structure has biological advantages in orthopedic implants: it has a lightweight design, provides a scaffold for bone ingrowth, and reduces metal artifacts during postoperative surveillance for local recurrence[16,19]. Providing an appropriate pore structure is the most important factor when using mesh structures to enhance osteointegration. A few animal studies have reported the osteoinductive effect of 3D-printed titanium alloy implants[20-24], and one human case study reported 8%–10% bone integration into the mesh structure[25]. The mesh structure is commonly mentioned in previous literature on 3D-printed custom-made implants in orthopedic oncology, particularly at the bone and implant junctions, because it provides a scaffold for bone ingrowth[11,15,16,19]. However, the lattice structure shows mechanical weakness compared to the solid structure, and the roughness of the lattice structure may cause irreparable damage to neurovascular structures[26]. Therefore, a lattice structure is combined with a solid structure rather than used alone.

Various specimens have been studied to optimize implant structures. Nevertheless, to our knowledge, only specimens with cross-sectional symmetry with respect to the longitudinal axis have been studied to optimize orthopedic implants. For instance, a fully lattice implant with cross-sectional symmetry has been studied to achieve the desired light weight and compatible mechanical properties compared to bone structures[27]. In addition, a fully lattice implant with a gradient macrostructure is utilized in bone implants, and the mechanical properties of these structures have been reported[27-29]. Bone tissue in nature has a structural gradient. If the lattice structure implant does not mimic these gradients, stress shielding occurs owing to uneven load distribution, resulting in resorption and bone failure of host tissues. In most orthopedic surgeries using 3D-printed implants, hybrid implants, rather than fully lattice implants, are utilized. Several studies have also been conducted to control the porosity, pore size, and shape of hybrid implants using compressive and tensile tests[30]. While these studies have been conducted on specimens with cross-sectional symmetry, in actual surgical cases, implants have complex surfaces with an asymmetric section, as shown in Figure 1, for the purpose of ensuring sufficient mechanical strength and avoiding damage major neurovascular structure. Thus, studies on such hybrid implants, including pizza types (P-type) and shell types (S-type), should be carried out.

Common mixing patterns with lattice and solid structures can be categorized into two types. One mixing pattern was a lattice coating with a solid core in the center (Figure 1a). In another pattern, the two structures occupy a certain volume without a central core structure (Figure 1b). The S-type is often utilized in limb salvage surgery for long bones, while the P-type is applied for flat bones, such as pelvic bones. However, there are no specific mechanical analyses or guidelines for combining lattice and solid structures to design a mechanically durable megaprosthesis.

Before limb salvage surgery, the mechanical properties of the 3D-printed implant, including the hybrid structure with solid and lattice structures, should be evaluated preoperatively experimentally to ensure that it will last for the entire lifetime of the patient, given the diverse shapes and proportions of hybrid structures in each surgery. However, it is practically impossible to evaluate the personalized types of implants experimentally owing to the absence of standard design criteria for the implant and time limitation that inevitably arise because bone tumors are progressing over time. Therefore, finite element analysis (FEA) is required to replace the experiment.

The present study entailed mechanical and microstructural analyses for Ti-6Al-4V solid-mesh hybrid structures produced by electron beam melting (EBM). Different types of hybrid structures with various

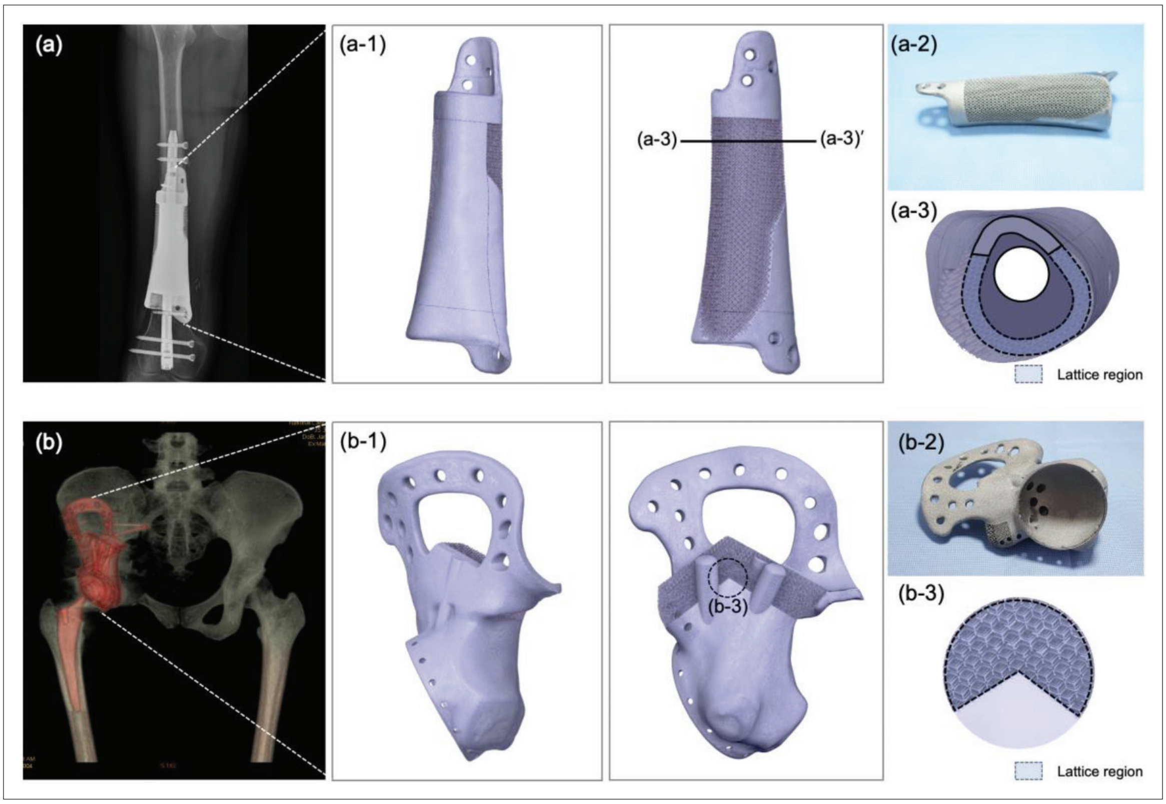

Figure 1. Ti-6AI-4V hybrid implant post-surgery. (a) Plain radiography (X-ray) of shell-type (S-type) and (b) computed tomography image of pizza-type (P-type). CAD images of (a-1) S-type and (b-1) P-type. Laboratory image of (a-2) S-type and (b-2) P-type. CAD images of (a-3) S-type region and (b-3) P-type region.

volume fractions of lattice structures were compared using experimental and computational analyses. The FEA results were validated using experimental data, and after the tensile test, microstructure analysis of the cross-sectional area of the specimens was conducted.

2. Experimental procedure

The test specimens were produced using an EBM-type 3D printer (ARCAM A1, GE Additive, USA), and the material was Ti-6Al-4V alloy powder (GE Additive, size 45–106 μm). The specimens were produced in adherence with the material's process conditions recommended by the manufacturer: electron beam power of 50–3000 W, beam current of 15 mA, speed factor of 60, scan speed of 4530 m/s, and layer thickness of 50 μm. Before investigating the mechanical properties of the hybrid structures, we examined the performance of the lattice structure by varying the size, build orientation, and unit cell orientation.

The dode-thin structure was chosen as the lattice structure because it is the only structure permitted under the national regulation for orthopedic implants. The unit cell sizes of the structures were 2 and 3 mm, respectively. There are three types of build orientation and two types of unit cell orientation. The build orientation was conducted as follows: horizontal (0°), diagonal (45°), and vertical (90°) directions with unit sizes of 2 and 3 mm, respectively, and the unit cell orientation was fixed. The unit cell orientation was carried out as follows: nonrotated unit cell and unit cell rotation of 45° with a horizontal build orientation, and the unit cell size was fixed at 2 mm.

The proposed hybrid structures were designed using the plan shown in Figure 2. The unit cell size was fixed at 2 mm in the horizontal direction. To evaluate the mechanical properties under the 3D printing process condition, the tensile specimens were fabricated according to the ASTM-E8 standard. Tensile tests were performed using an MTDI universal test machine with a load cell capacity of 100 kN under quasi-static conditions with a displacement control velocity of 3 mm/min. The specimens had lengths, diameters, and gauge lengths of 140 mm, 12.5 mm, and 50 mm, respectively. In order to investigate the mechanical behavior of the hybrid structure, the dode-thin type structure was applied along the gauge length of the specimens.

FEA was performed using commercial software (ANSYS Workbench Mechanical v19.1) to investigate the

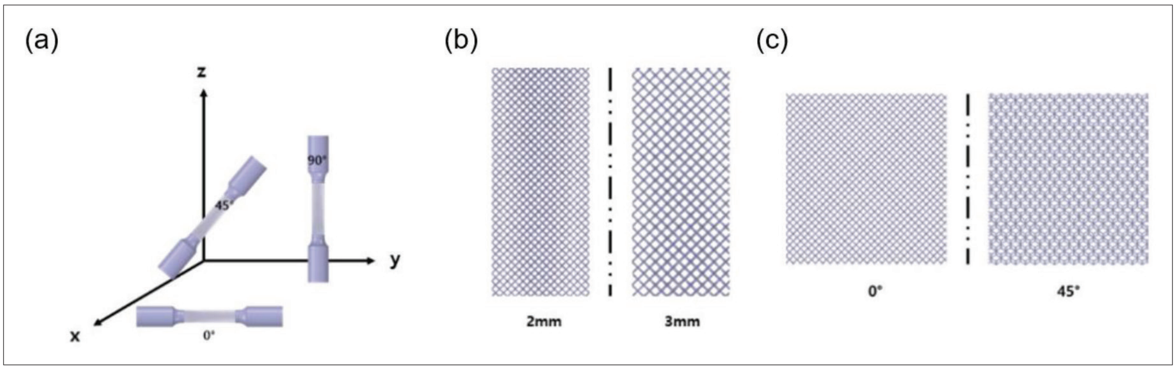

Figure 2. Schematic of lattice structure specimen. (a) Orientation; (b) unit cell size; (c) unit cell rotation.

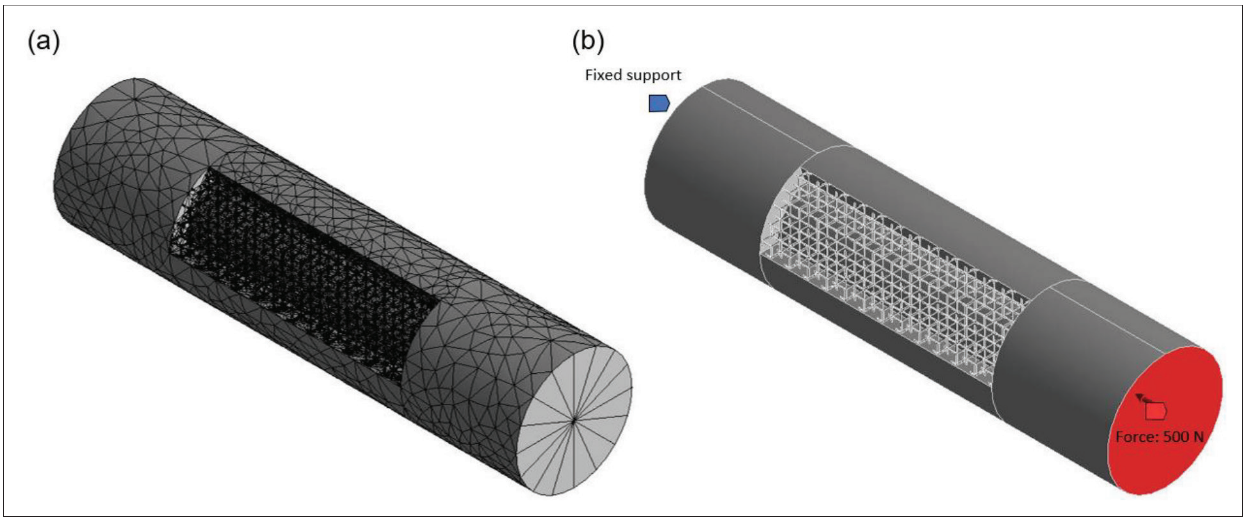

Figure 3. Boundary conditions for FEA results of hybrid structure with volume fraction 10%. (a) Mesh generation. (b) Fixed support and load conditions.

characteristics of the designed hybrid models. To reduce computational time, the symmetry condition was applied to the hybrid structure specimens' centerline, the end of the specimen surface at gauge length was fixed, and a uniform compressive load of 500 N was applied to the specimen grip (Figure 3). In addition, for the calibration of the FEA model, maximum von Mises stress and displacements were tested under load conditions of 400 N and 600 N (Tables 1 and 2). For hybrid specimens, meshes with 1,500,000–5,700,000 tetrahedral solid-type elements were used, and the element size was 2.6448 mm. Using the material designer in ANSYS, the following Ti alloy properties were calculated for the lattice structure: $\rho = 0.18$ g/cm^3, $E = 41.65$ MPa for elastic modulus, and $\nu = 0.486$ for Poisson's ratio.

3. Results and discussion

The simulation results for the lattice structures with various unit sizes and rotated unit cell directions are shown in Figure 4. The von Mises stress increases as the unit size increases and decreases as the unit cell is rotated. The von Mises stress of the 3 mm/0° lattice structure was the highest at 1611 MPa, and that of the 2 mm/45° lattice structure was the lowest at 1456 MPa. While the yield strength of EBM Ti-6Al-4V is about 915–1200 MPa[31], the three lattice structures have higher maximum von Mises stress. These FEA results show that the three fully porous designs are unsustainable for compression of 500 N, thus it is essential to have solid-porous mixed hybrid structure rather than pure porous structure. Consequently, the 2 mm/45° lattice structure would be preferable for the hybrid structure. However, implants are not as standardized as specimens in actual orthopedic surgery. In other words, unit cell orientation and building axis for the lattice structure cannot be controlled when the lattice is used as part of a real implant. Therefore, the direction of the applied force is not constant, and the unit cell direction of the specimen cannot be determined. For the worst-case testing of the 2 mm lattice structure, we applied the 2 mm/0° lattice structure to all hybrid structures to evaluate their performance.

Table 1. FEA results for maximum von Mises stress under various loading conditions

Specimens	Maximum von Mises stress (MPa)		
	400 N	500 N	600 N
P-type 20%	37.0	46.2	55.5
P-type 40%	79.6	99.5	119.4
P-type 60%	273.9	342.3	410.8
P-type 80%	769.3	961.6	1154.0
P-type 100%	1495.9	1525.3	1563.8
S-type 10%	30.3	37.9	45.5
S-type 20%	36.9	46.2	55.4
S-type 30%	48.2	60.5	72.3
S-type 40%	44.7	55.9	67.0
S-type 50%	46.0	57.5	69.0

Table 2. FEA results for displacements under various loading conditions

Specimens	Displacements (μm)		
	400 N	500 N	600 N
P-type 20%	4.5	6.2	7.5
P-type 40%	22.8	28.5	34.3
P-type 60%	85.3	106.6	127.9
P-type 80%	205.3	256.6	308.0
P-type 100%	770.3	1044.2	1610.1
S-type 10%	2.8	3.5	4.2
S-type 20%	5.1	6.4	7.7
S-type 30%	5.9	7.4	8.9
S-type 40%	5.0	6.3	7.6
S-type 50%	2.4	3.0	3.6

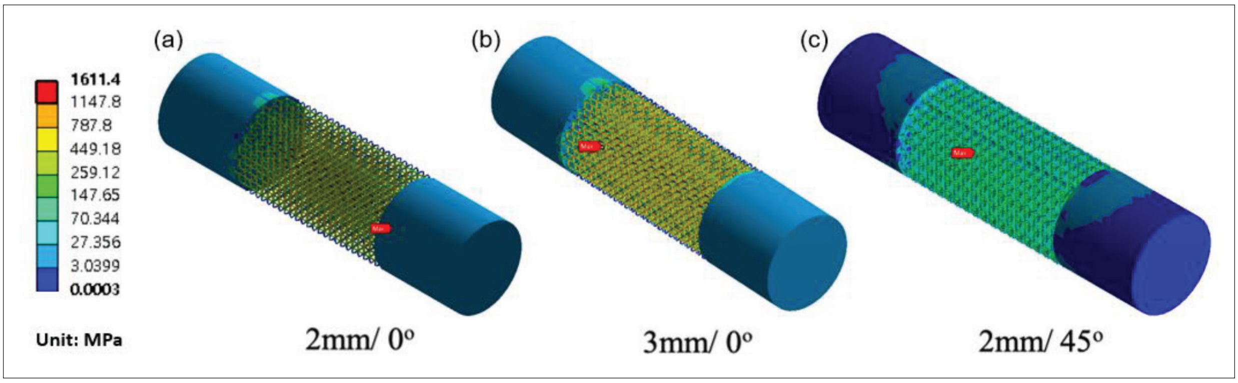

Figure 4. FEA results for the lattice structure with different sizes and unit cell rotation. (a) 2 mm with 0° (1525 MPa); (b) 3 mm with 0° (1611 MPa); (c) 2 mm with 45° (1456 MPa).

The cross-section illustration of P- and S-type hybrid structures for the volume fraction of the lattice structure is shown in Figure 5. P- and S-type specimens analyzed under a load of 500 N, which was determined considering the weight of an average human. The P-type hybrid structure was simulated with various volume fractions of 20%–100%, respectively (Figure 6). The maximum von Mises stress increased as the volume fraction of the lattice structure increased. When the volume fraction is 20%, the maximum von Mises stress is 46.2 MPa. Up to 40% of the volume fraction, the maximum von Mises stress shows a small increase of less than 100 MPa. However, from 60% of the volume fraction, the maximum von Mises stress increased significantly. When the volume fraction is 60%, it is 342.3 MPa, and when the volume fraction is 100%, it is 961.6 MPa, which increases more than two times compared to the previous case.

Figure 7 shows the simulation results for the S-type hybrid structure with various volume fractions of 10%–50%, respectively. In the case of S-type, since 50% of solid beam exists inside, the volume fraction of the lattice structure was set to 10%–50%. When the volume fraction is 20%, the maximum von Mises stress is 46.2 MPa, which is similar to the results for the P-type. However, when the volume fraction is 40%, the maximum von Mises stress is 55.9 MPa, which is much lower than the result of the P-type with 99.5 MPa. In addition, in the case of the S-type, the maximum von Mises stress did not increase rapidly even when the volume fraction was increased to 50%, whereas in the case of the P-type, it increased rapidly when the volume fraction was increased to 60% (Figure 8). In particular, the maximum von Mises stress at 50% volume fraction for the S-type was 57 MPa, while it exceeded 300 MPa for the P-type at a volume fraction of 60%. As a result of FEA simulations, the maximum von Mises stress was similar when the volume fraction of lattice structure was low in both P- and S-type, but in the case of P-type, it increased rapidly as the volume fraction increased.

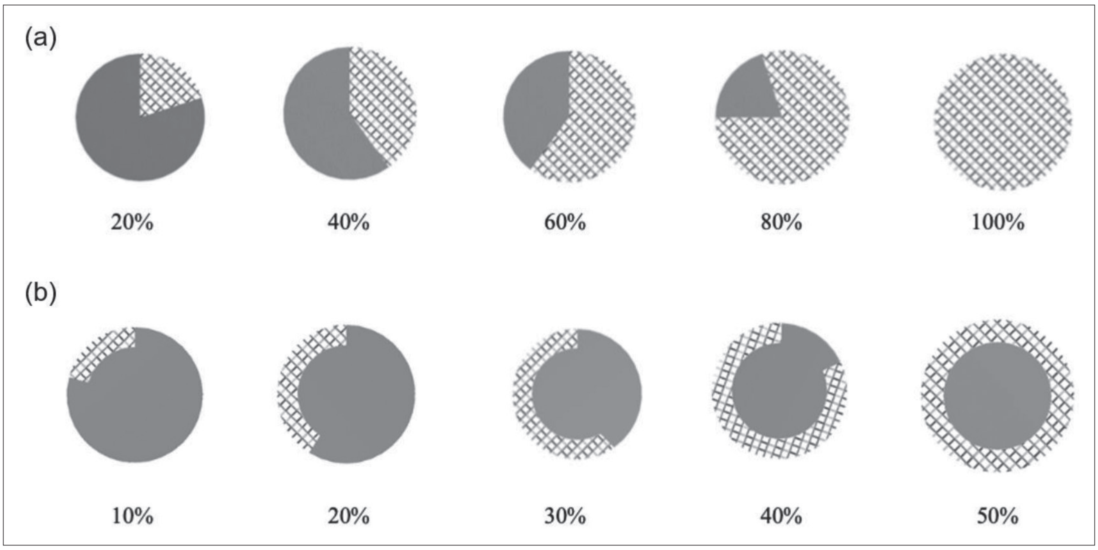

Figure 5. Illustration of hybrid structures for the volume fraction of lattice structure. (a) P-type; (b) S-type.

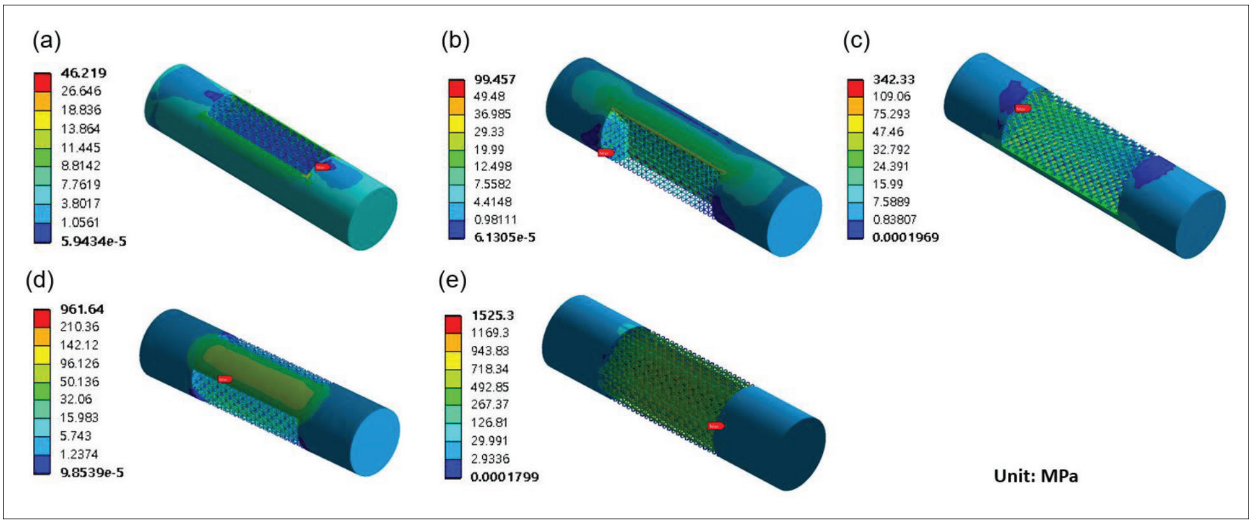

Figure 6. FEA direct analysis results for P-type hybrid structures with different fractions. (a) 20%; (b) 40%; (c) 60%; (d) 80%; (e) 100%.

The experimental results from the tensile test were compared with the FEA simulations to validate the analysis approach. Figure 9 shows the tensile properties of the hybrid and lattice-type structure specimens, and the corresponding property values are listed in Table 3. The tensile strength of the hybrid structure specimens decreased as the mesh volume fraction increased. The pure lattice structure specimen had the lowest strength compared with the other hybrid structure specimens. In the S-type specimen, the elongation increased as the mesh volume fraction increased, except for the 10% specimen. S-type 10% specimen showed the highest strength and elongation owing to the lowest mesh volume fraction. However, the elongation of the P-type specimens decreased as the mesh volume fraction increased, except for the 20% specimen, which exhibited the lowest mesh volume fraction. Figure 9b shows that the tensile strength of the S-type specimen is always higher than that of the P-type specimen when the mesh volume fraction is held constant. In particular, when the mesh volume fraction was 40%, the tensile strength of the S-type specimen was 600 MPa, whereas that of the P-type was 567 MPa. We suggest an empirical equation (see Equation I) to satisfy the relationship between the mesh volume fraction and tensile strength for application in this study.

$$\sigma_{TS} = -1479 + 68573 / \left(1 + \exp\frac{\left(f_{mesh} + 690\right)}{210}\right) \qquad \text{(I)}$$

where σ_{TS} is the tensile strength and f_{mesh} is the mesh volume fraction. Regardless of the P- or S-type, tensile

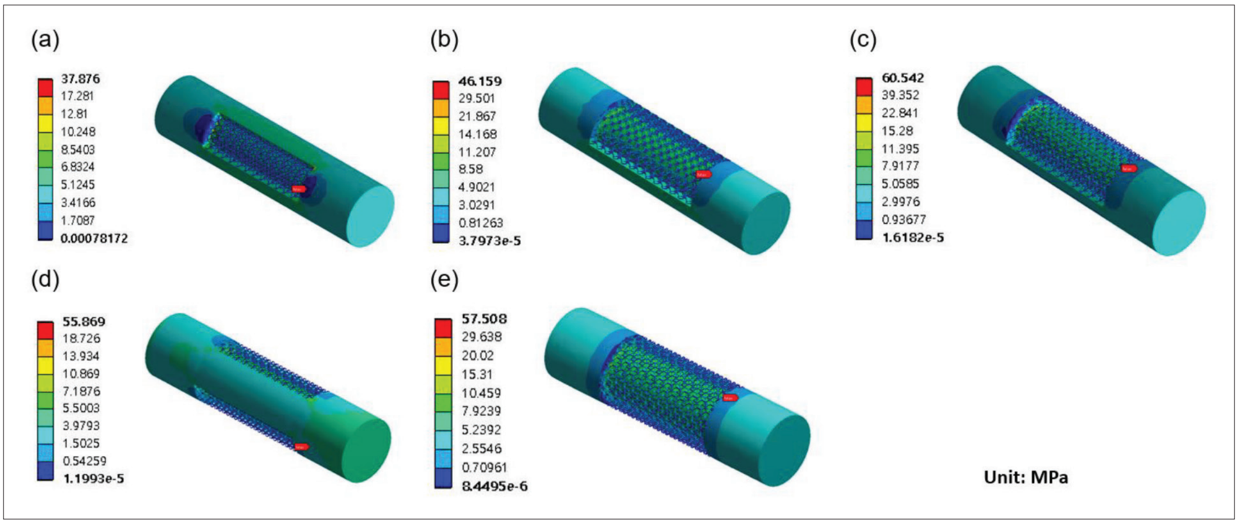

Figure 7. FEA direct analysis results for S-type hybrid structures with different fractions. (a) 10%; (b) 20%; (c) 30%; (d) 40%; (e) 50%.

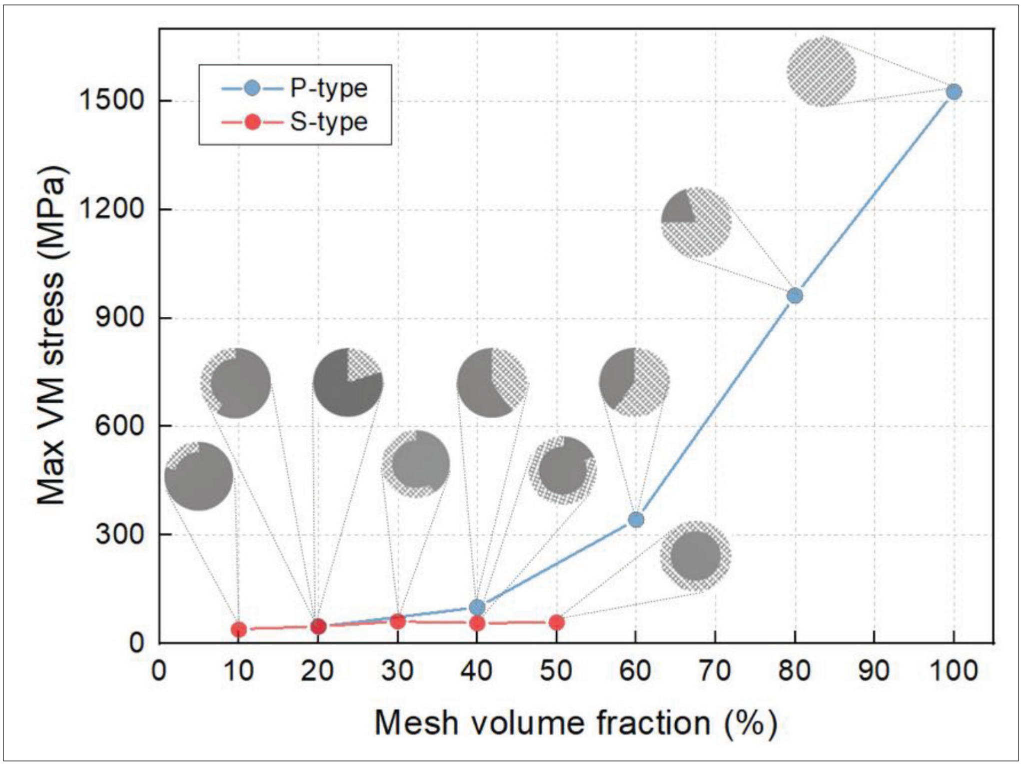

Figure 8. Maximum von Mises stress with 500 N for P-type and S-type specimens.

strength exponentially depended on mesh volume fraction (Figure 9b). In practical point of view, implant strength is more important than bone and tissue ingrowth. Therefore, even if the lattice structure is used for the purpose of osseointegration or to reduce stress shielding, the fact that the strength of the hybrid structure decreases by the cross-sectional volume fraction of the lattice structure should be taken into account in the design process. In particular, the long bones in the lower extremities and pelvis play a crucial role in weight-bearing and thus, it is important to accurately determine their volume fraction of the lattice structure.

The fractography of the hybrid structure specimens after tensile testing is shown in Figure 10. The fractographic surface in the solid region is divided into stage 1 with crack initiation and growth (orange) and stage 2 with shear fracture (blue).

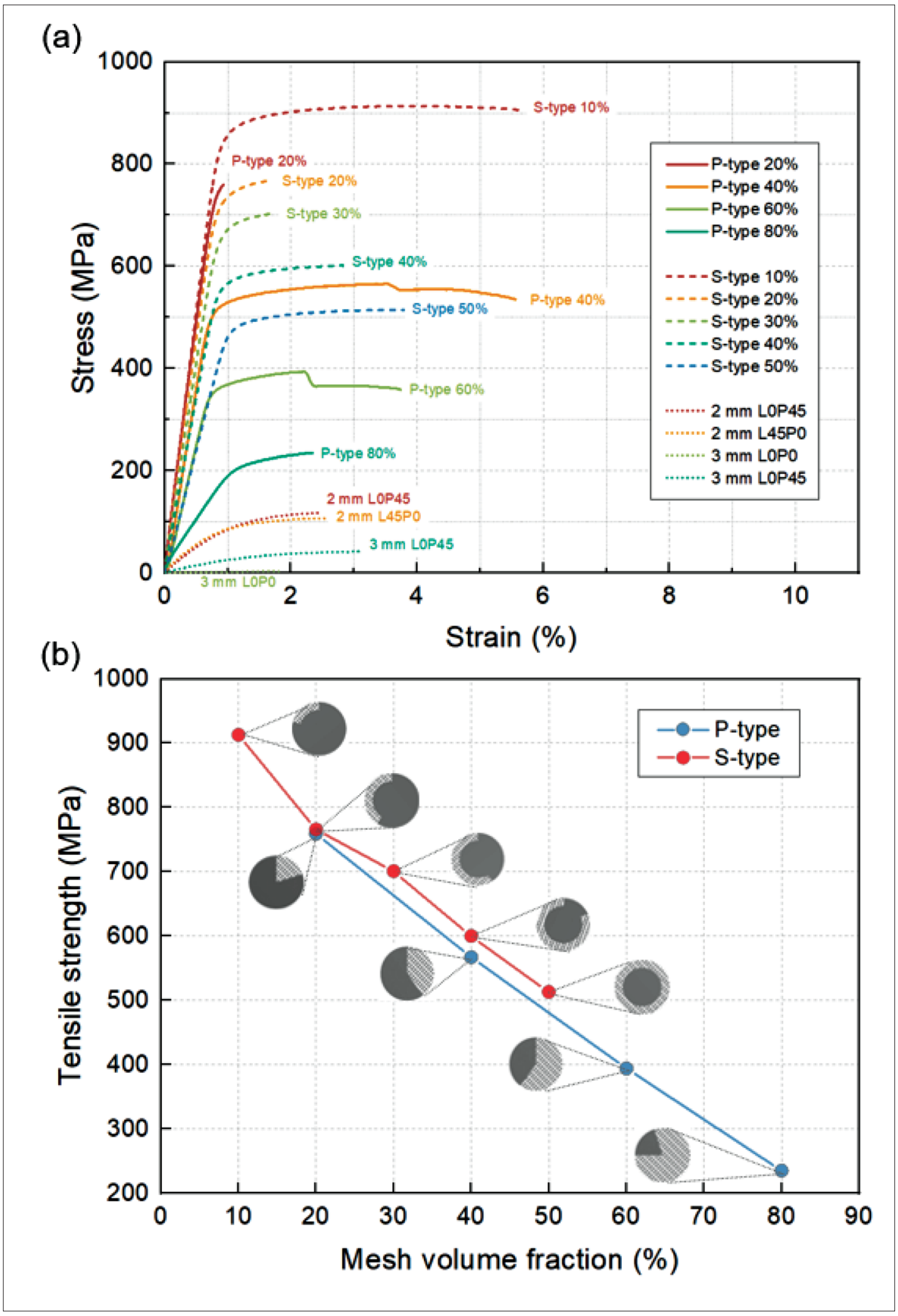

Figure 9. Experimental tensile test results of hybrid structures. (a) Engineering stress–strain curve of each structure specimen tensile-tested at room temperature (strain rate of 1×10^{-3}/s). (b) Tensile strength with different mesh volume fractions for each type.

Stage 1 is starting from the center of the specimen having flat and plateau surface, while stage 2 is a shear lip with slanting ridge along the rim of the specimen. In general, shear lip has a 45° angle to the loading axis formed by plane stress condition near surface. In Table 4, the volume fractions of stages 1 and 2 areas were measured from the cross-section of the entire specimen. Crack is initiated in the center of the solid part that stress is localized by plane strain condition at the stage 1. The coarsened voids are merged with the adjacent voids, which lead to form main cracks. The stage 2 is formed by shear fracture mode affected by plane stress condition. The volume fraction of each stage varies with the specimens, and the volume fraction of stage 1 shows the close relationship to the tensile strength comparing to that of stage 2. Therefore, cracking behavior has a huge influence on the tensile strength of the specimens.

Table 3. Tensile test results of P-type and S-type specimens.

Specimens	Yield strength (MPa)	Tensile strength (MPa)	Elongation (%)	Max von Mises stress (MPa)
P-type 20% 2 mm	–	759	0.9	46.2
P-type 40% 2 mm	525	567	3.8	99.5
P-type 60% 2 mm	364	394	2.4	342.3
P-type 80% 2 mm	211	235	2.4	961.6
S-type 10% 2 mm	863	913	5.7	37.9
S-type 20% 2 mm	734	766	1.7	46.2
S-type 30% 2 mm	674	701	1.7	60.5
S-type 40% 2 mm	566	600	2.8	55.9
S-type 50% 2 mm	483	513	3.9	57.5
2mm L0P45	85	117	2.4	–
2mm L45P0	81	107	2.6	–
3mm L0P0	2.5	3.0	2.6	–
3mm L0P45	27	42	3.1	–

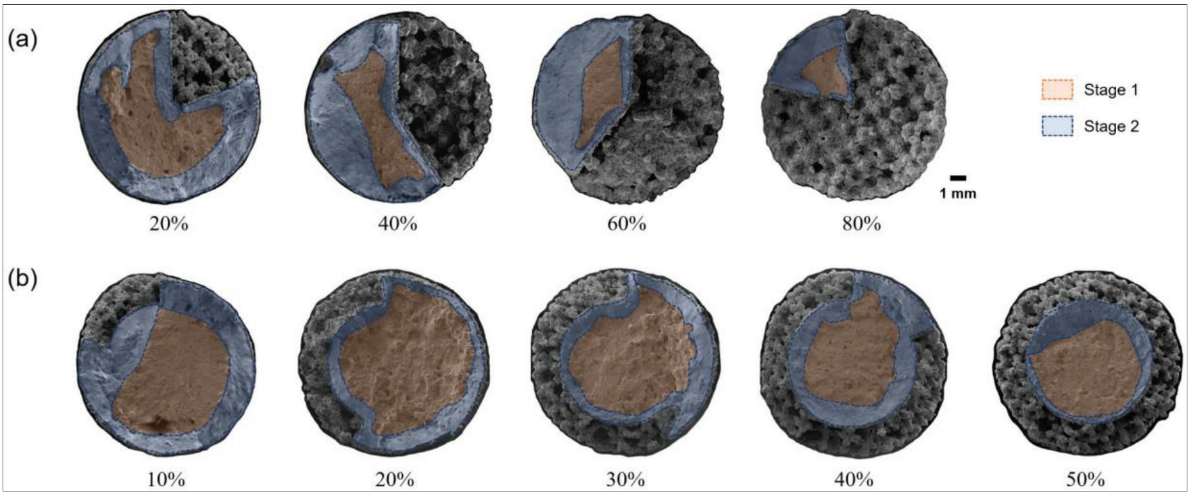

Figure 10. Fractography of hybrid structures after tensile test. Low-magnification fractography of (a) P-type and (b) S-type specimens.

Figure 10 depicts the low-magnification fractography of hybrid structures after the tensile test for P- and S-type specimens, while Figure 11 shows the fractographic analysis with the same mesh volume fraction of 40%. In both specimens, fracture occurred at the center of the solid region, whereas shear fracture occurred at the rim of the solid region. At the interface between the solid and mesh regions, large pores were mainly formed, which acted as crack initiation sites. Figure 10 shows that deep and clear dimples were observed in stage 1, while shallow dimples were formed in stage 2. The S-type specimen had higher strength and lower elongation than the P-type specimen owing to the large volume fraction of the stage 1 area (orange) (Figure 9). The stage 1 area volume fractions were calculated as 15.1% and 25.7% in the P- and S-type specimens, respectively. Therefore, the high strength of the

Table 4. Volume fraction of the shear lip region in each specimen

Specimens	Area fraction (%)		Tensile strength (MPa)
	Stage 1	Stage 2	
P-type 20%	29.7	43.3	759
P-type 40%	15.1	36.5	567
P-type 60%	9.3	25.8	394
P-type 80%	4.7	11.4	235
S-type 10%	37.7	28.1	913
S-type 20%	46.6	13.6	766
S-type 30%	36.1	15.1	701
S-type 40%	25.7	18.0	600
S-type 50%	26.3	10.4	513

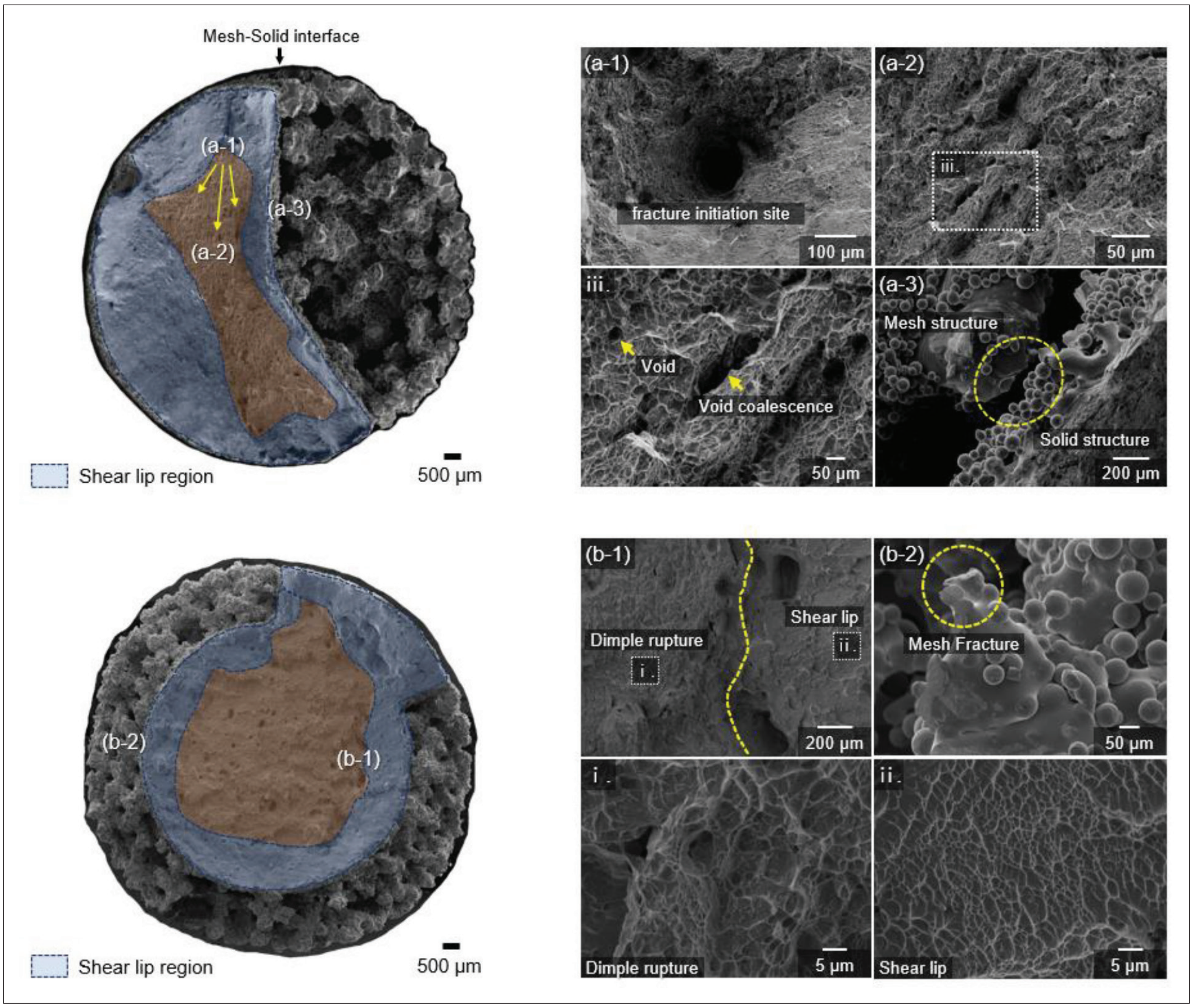

Figure 11. Fractography of (a) P-type and (b) S-type specimens of mesh volume fraction of 40%. High-magnification image of (a-1, -2, -3) P-type and (b-1, -2) S-type specimens.

S-type specimen was achieved by the large volume fraction of the stage 1 area.

The electron backscatter diffraction (EBSD) results for the cross-sectional area after the tensile test (Figure 12), and the specimens were extracted from the solid and mesh interface regions, as shown in Figure 11a and b. The columnar β cell is formed along the build direction surrounding the acicular α' martensite. Both specimens were composed of α' martensite structures owing to the fast cooling rate during solidification. The lath width is similar between the solid region (3.49 μm) and the mesh region (3.74 μm) in the P-type specimen. However, in the S-type specimen, the lath width was finer in the mesh region (1.84 μm) than in the solid region (3.74 μm). In the P-type specimen, the interface between the solid and mesh is located in the center of the specimen.

In contrast, it is located in the vicinity of the rim area in the S-type specimen (Figure 5). A fine microstructure can be obtained owing to the high-temperature gradient near the surface during cooling[1]. The cooling rate in the mesh structure is much higher than that in the solid structure; thus, fine acicular α' martensite aiding in increasing the tensile strength was formed in the mesh structure of the S-type specimen.

Combining the mechanical, computational, and microstructural results, the S-type was more suitable for bone replacement implants than the P-type. In the tensile test, the mechanical performance of the S-type was superior to that of the P-type at the same volume fraction of lattice structures. The FEA results of the P-type show that the maximum von Mises stress increased significantly as the volume fraction increased. In addition, it was confirmed

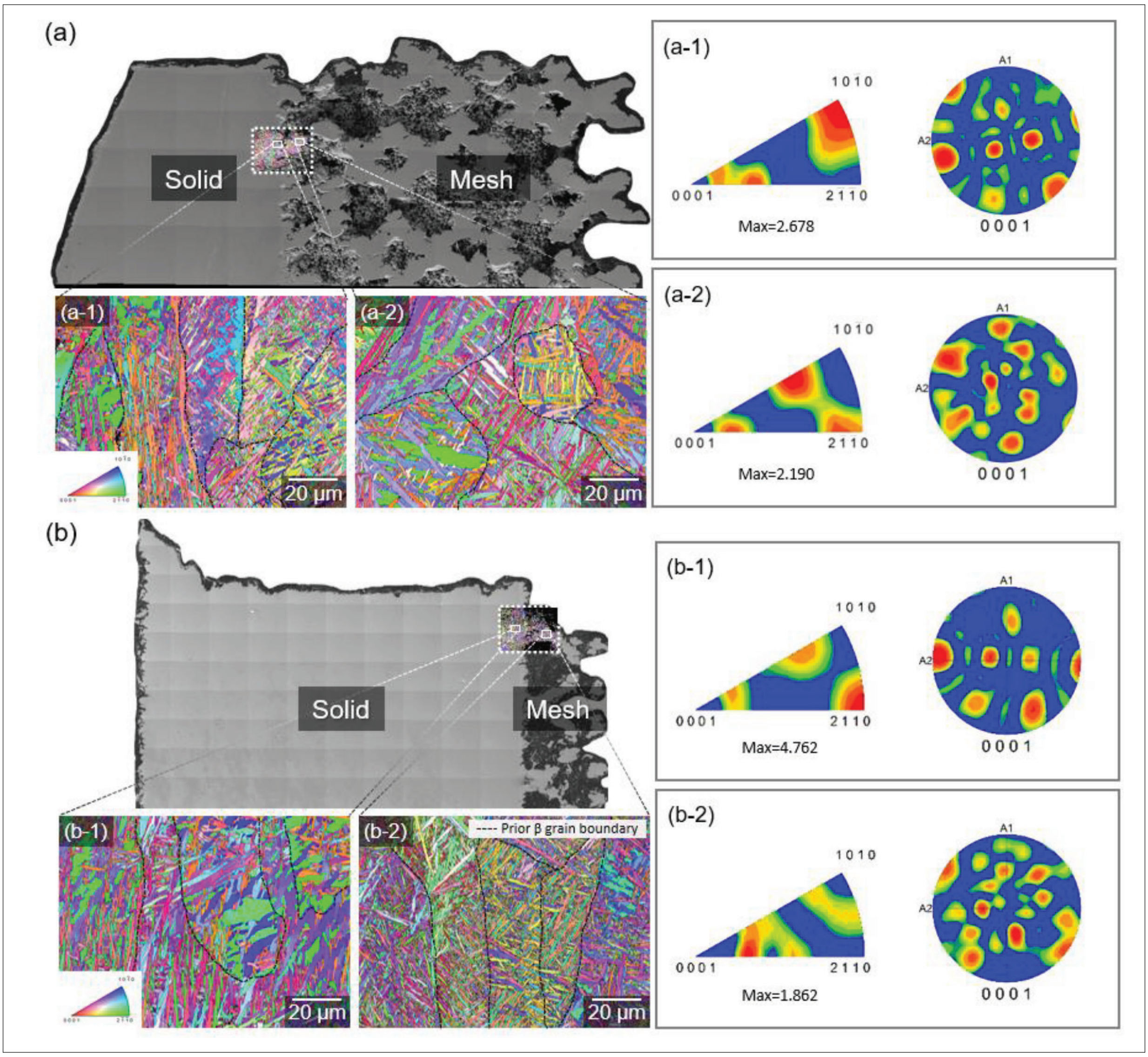

Figure 12. Cross-sectional EBSD analysis of tensile test fractured (a) P-type 40% and (b) S-type 40% specimens. Inverse pole figure map and texture analysis results of (a-1) solid and (a-2) mesh region in P-type specimen. Inverse pole figure map and texture analysis results of (b-1) solid and (b-2) mesh region in S-type specimen. Texture analysis of (c) P-type 40% and (d) S-type 40% specimens.

that the S-type had higher tensile strength than the P-type in EBSD results and fractional analysis.

4. Conclusion

The mechanical behavior of Ti-6Al-4V specimens with the proposed hybrid structures produced by EBM was tested and simulated. We compared two types of hybrid structures and validated the FEA results with the experimental data. Based on the FEA results, the maximum von Mises stress increases as the volume fraction of the lattice structure increases. Analysis of the tensile test also showed that the mechanical performance tends to decrease as the volume fraction of the lattice structures increases. The fractography results showed that the tensile strength increases with increasing volume fraction of the solid region composed of stages 1 and 2, regardless of the specimen type.

In a tensile test, the performance of the shell design was superior to that of the P-type with the same volume fraction of lattice structures. The P- and S-types were analyzed using EBSD results and fractographic analysis. After the tensile test, the EBSD results for the cross-sectional area of the S-type specimen revealed that the lath width was finer in the mesh region than in the solid region. In contrast, the P-type specimen's lath widths were similar. Fine acicular α' martensite observed in the S-type mesh region is generated at high-temperature gradients near the rim and high cooling rates of the mesh structures, thereby increasing the tensile strength of the specimen. In addition, the results of the fractographic analysis of P- and S-type specimens with the same mesh volume fraction indicate that the high strength of the S-type specimen was achieved by the large volume fraction of the stage 1 area, where deep and clear dimples were observed.

Through patient-specific orthopedic implants with an optimized volume fraction of the lattice structure, mechanical performance for repeated weight loading was improved, and guidelines for implant design could be established. However, it is necessary to devise definitive implant designs that are clinically safe, and thus provide a range of clear volume fractions of lattice structures. Moreover, further works on fatigue behavior upon repetitive loads applied to the lower limbs are also necessary. These results and continuous research can provide a better basis for effective enhancement of mechanical performance and optimized safe designs.

Acknowledgments

None.

Funding

This work was supported by the Technology Innovation Program (grant no. 20017502) funded by the Ministry of Trade, Industry & Energy (MOTIE, Korea), the National Research Foundation of Korea (NRF) grant funded by the Korea government (MSIT) (grant no. 2021M2D2A1A01050059, 2020R1C1C1006214), and the research grant funded by the National Cancer Center of the Republic of Korea (grant no. 2110270).

Conflict of interest

The authors declare that they have no known competing financial interests or personal relationships that could have appeared to influence the work reported in this paper.

Author contributions

Conceptualization: Jong Woong Park, Eunhyeok Seo, Hyokyung Sung, Im Doo Jung
Formal analysis: Jong Woong Park, Eunhyeok Seo, Haeum Park, Ye Chan Shin, Hyokyung Sung, Im Doo Jung
Funding acquisition: Hyokyung Sung, Im Doo Jung
Investigation: Jong Woong Park, Eunhyeok Seo, Haeum Park, Ye Chan Shin
Methodology: Haeum Park, Ye Chan Shin, Hyun Guy Kang
Supervision: Hyokyung Sung, Im Doo Jung
Visualization: Jong Woong Park, Eunhyeok Seo, Hyun Guy Kang
Writing – original draft: Jong Woong Park, Eunhyeok Seo, Hyokyung Sung, Im Doo Jung
Writing – review & editing: Jong Woong Park, Eunhyeok Seo, Hyun Guy Kang, Hyokyung Sung, Im Doo Jung

Ethics approval and consent to participate

Regarding the patient presented in Figure 1, this study protocol has been approved by the institutional review board of National Cancer Center (NCC2017-0129). The present study was conducted according to the principles of the Declaration of Helsinki. Written informed consent was obtained from a participant prior to inclusion in the study.

Consent for publication

Not applicable.

Availability of data

Not applicable.

References

1. Mankin H, Gebhardt M, Jennings L, *et al.*, 1996, Long-term results of allograft replacement in the management of bone tumors. *Relat Res*, 324:86–97.

2. Wunder J, Leitch K, Griffin A, *et al.*, 2001, Comparison of two methods of reconstruction for primary malignant tumors at the knee: A sequential cohort study. *J Surg Oncol*, 77:89–99.

   https://doi.org/10.1002/jso.1076

3. Jeon DG, Kim MS, Cho WH, *et al.*, 2007, Pasteurized autograft for intercalary reconstruction. *Clin Orthop Relat Res*, 456:203–210.

   https://doi.org/10.1097/BLO.0b013e31802e7ec8

4. Jeon DG, Song WS, Cho WH, *et al.*, 2014, Overlapping allograft for primary or salvage bone tumor reconstruction. *J Surg Oncol*, 110:366–371.

   https://doi.org/10.1002/jso.23669

5. Shusteff M, Browar AEM, Kelly EW, *et al.*, 2017, One-step volumetric additive manufacturing of complex polymer structures. *Sci Adv*, 3:eaao5496.

   https://doi.org/10.1126/sciadv.aao5496

6. Zhang D, Qiu D, Gibson MA, *et al.*, 2019, Additive manufacturing of ultrafine-grained high-strength titanium alloys. *Nature*, 576:91–95.

   https://doi.org/10.1038/s41586-019-1783-1

7. Jung ID, Choe J, Yun J, *et al.*, 2019, Dual speed laser re-melting for high densification in H13 tool steel metal 3D printing. *Arch Metall Mater*, 64(2):571–578.

   https://doi.org/10.24425/amm.2021.136388

8. Sing SL, 2022, Perspectives on additive manufacturing enabled beta-titanium alloys for biomedical applications. *Int J Bioprint*, 8(1):478.

http://dx.doi.org/10.18063/ijb.v8i1.478

9. Lee MS, Kim H, Koo YT, *et al.*, 2022, Selective laser melting process for sensor embedding into SUS316L with heat dissipative inner cavity design. *Met Mater Int*, 28:297–305.

https://doi.org/10.1007/s12540-021-01106-3

10. Wong KC, Kumta SM, Geel NV, *et al.*, 2015, One-step reconstruction with a 3D-printed, biomechanically evaluated custom implant after complex pelvic tumor resection. *Aided Surg*, 20:14–23.

https://doi.org/10.3109/10929088.2015.1076039

11. Liang H, Ji T, Zhang Y, *et al.*, 2017, Reconstruction with 3D-printed pelvic endoprostheses after resection of a pelvic tumour. *Bone Jt J*, 99-B:267–275.

https://doi.org/10.1302/0301-620X.99B2.BJJ-2016-0654.R1

12. Wei R, Guo W, Ji T, *et al.*, 2017, One-step reconstruction with a 3D-printed, custom-made prosthesis after total en bloc sacrectomy: A technical note. *Eur Spine J*, 26:1902–1909.

https://doi.org/10.1007/s00586-016-4871-z

13. Park JW, Kang HG, Lim KM, *et al.*, 2018, Three-dimensionally printed personalized implant design and reconstructive surgery for a bone tumor of the calcaneus. *JBJS Case Connect*, 8:e25.

https://doi.org/10.2106/JBJS.CC.17.00212

14. Park JW, Kang HG, Lim KM, *et al.*, 2018, Bone tumor resection guide using three-dimensional printing for limb salvage surgery. *J Surg Oncol*, 118:898–905.

https://doi.org/10.1002/jso.25236

15. Angelini A, Trovarelli G, Berizzi A, *et al.*, 2019, Three-dimension-printed custom-made prosthetic reconstructions: From revision surgery to oncologic reconstructions. *Int Orthop*, 43:123–132.

https://doi.org/10.1007/s00264-018-4232-0

16. Park JW, Kang HG, Kim JH, *et al.*, 2020, New 3-dimensional implant application as an alternative to allograft in limb salvage surgery: A technical note on 10 cases. *Acta Orthop*, 91:489–496.

https://doi.org/10.1080/17453674.2020.1755543

17. Eleutério SJP, Senerchia AA, Almeida, *et al.*, 2015, Osteosarcoma in patients younger than 12 years old without metastases have similar prognosis as adolescent and young adults. *Pediatr Blood Cancer*, 62:1209–1213.

https://doi.org/10.1002/pbc.25459

18. Kim Y, Jang WY, Park JW, *et al.*, 2020, Transepiphyseal resection for osteosarcoma in patients with open physes using MRI assessment. *Bone Jt J,* 102-B:772–778.

https://doi.org/10.1302/0301-620X.102B6.BJJ-2019-1141.R2

19. Park JW, Kang HG, Kim JH, *et al.*, 2021, The application of 3D-printing technology in pelvic bone tumor surgery. *J Orthop Sci*, 26(2):276–283.

https://doi.org/10.1016/j.jos.2020.03.004

20. Mumith A, Coathup M, Chimutengwende-Gordon M, *et al.*, 2017, Augmenting the osseointegration of endoprostheses using laser-sintered porous collars. *Bone Jt J*, 99-B:276–282.

https://doi.org/10.1302/0301-620X.99B2.BJJ-2016-0584.R1

21. McGilvray KC, Easley J, Seim HB, *et al.*, 2018, Bony ingrowth potential of 3D-printed porous titanium alloy: A direct comparison of interbody cage materials in an in vivo ovine lumbar fusion model. *Spine J*, 18(7):1250–1260.

https://doi.org/10.1016/j.spinee.2018.02.018

22. Wu SH, Li Y, Zhang YQ, *et al.*, 2013, Porous titanium-6 aluminum-4 vanadium cage has better osseointegration and less micromotion than a poly-ether-ether-ketone cage in sheep vertebral fusion. *Artif Organs*, 37:E191–E201.

https://doi.org/10.1111/aor.12153

23. Li JP, Habibovic P, Van Den Doel M, *et al.*, 2007, Bone ingrowth in porous titanium implants produced by 3D fiber deposition. *Biomaterials*, 28:2810–2820.

https://doi.org/10.1016/j.biomaterials.2007.02.020

24. De Wild M, Zimmermann S, Rüegg J, *et al.*, 2016, Influence of microarchitecture on osteoconduction and mechanics of porous titanium scaffolds generated by selective laser melting. *3D Print Addit Manuf*, 3(3):142–151.

https://doi.org/10.1089/3dp.2016.0004

25. Park JW, Song CA, Kang HG, *et al.*, 2020, Integration of a three-dimensional-printed titanium implant in human tissues: Case study. *Appl Sci*, 10:553.

https://doi.org/10.3390/app10020553

26. Park JW, Shin YC, Kang HG, *et al.*, 2021, In vivo analysis of post-joint-preserving surgery fracture of 3D-printed Ti-6Al-4V implant to treat bone cancer. *Bio-des Manuf*, 4:879–888.

https://doi.org/10.1007/s42242-021-00147-2

27. Limmahakhun S, Oloyede A, Sitthiseripratip K, *et al.*, 2017, Stiffness and strength tailoring of cobalt chromium graded cellular structures for stress-shielding reduction. *Mater Des*, 114:633–641.

https://doi.org/10.1016/j.matdes.2016.11.090

28. Mahmoud D, Elbestawi MA, 2019, Selective laser melting of porosity graded lattice structures for bone implants. *Int J Adv Manuf*, 100:2915–2927.

https://doi.org/10.1007/s00170-018-2886-9

29. Leong KF, Chua SC, Sudarmadji N, *et al.*, 2008, Engineering functionally graded tissue engineering scaffolds. *J Mech Behav Biomed Mater*, 1(2):140–152.

https://doi.org/10.1016/j.jmbbm.2007.11.002

30. Fousová M, Vojtěch D, Kubásek J, *et al.*, 2017, Promising characteristics of gradient porosity Ti-6Al-4V alloy prepared by SLM process. *Mech Behav Biomed Mater*, 69: 368–376.

https://doi.org/10.1016/j.jmbbm.2017.01.043

31. Sing SL, An J, Yeong WY, *et al.*, 2016, Laser and electron-beam powder-bed additive manufacturing of metallic implants: A review on processes, materials and designs. *J Orthop Res*, 34:369–385.

https://doi.org/10.1002/jor.23075